ARTICLE

Shape controlled assembly of carboxylic acids: formation of a binary monolayer by intercalation into molecular nanotunnels†

Received 00th January 20xx,
Accepted 00th January 20xx

DOI: 10.1039/x0xx00000x

Rodrigo Ortiz de la Morena,[a] Andika Asyuda,[b] Hao Lu,†[b] Hannah Aitchison,†[a] Kelly Turner,[a] Stephen M. Francis,[a] Michael Zharnikov[b] and Manfred Buck*[a]

Binary self-assembled monolayers (SAMs) combining a Y-shaped aromatic carboxylic acid (1,3,5-benzenetribenzoic acid, H3BTB) and a cage-type alicyclic carboxylic acid (adamantane carboxylic acid, AdCA) were investigated by scanning tunneling microscopy (STM), X-ray photoelectron spectroscopy (XPS), and X-ray absorption fine structure (NEXAFS) spectroscopy. The SAMs, prepared by molecular adsorption from solution on Au substrates modified by underpotential deposition of Ag, exhibit a pronounced depencence of their structure on the assembly protocol. Exposing an H3BTB SAM to AdCA, the highly regular row structure of the native H3BTB layer persists and STM imaging does not show signs of AdCA adsorption. This is in striking contrast to the disordered arrangements of H3BTB and the presence of AdCA employing the inverted adsorption sequence or coadsorption of the two molecules. However, spectroscopic analysis of the H3BTB SAM exposed to AdCA reveals the presence also of the latter, suggesting that the AdCA molecules are hidden in the nanotunnels of the H3BTB monolayer. Additional evidence for the intercalation of AdCA is obtained by STM manipulation experiments which lay bare areas of AdCA molecules upon local removal of H3BTB. Surprisingly, these are densely packed and arranged into a highly ordered monolayer. Formation of such a compact AdCA layer is explained by expulsion of AdCA from the H3BTB nanotunnels of the surrounding intact mixed SAM, driven by release of stress in the nanotunnels built up when AdCA is intercalated.

Introduction

Two component self-assembled monolayers (SAMs) as a means of tuning interfacial properties are of interest for a number of rather different reasons[1] as illustrated by the control of wetting,[2-6] reduction of sterical hindrance impeding chemical reactivity[7-9] and photoswitching,[10,11] increase of sensitivity and specificity of sensors,[12,13] or modification of the work function of an electrode to improve charge injection in organic electronic devices.[14-18]

Mixed SAMs are prepared by either coadsorption or sequential adsorption of the components which, on the one hand, is a very simple protocol but, on the other hand, limits the level of control as layers result with a statistical distribution of components which, depending on intermolecular interactions, is expressed on different length scales. If the interactions are similar between like and unlike molecules they can mix randomly on the molecular length scale[19,20] whereas substantial differences in the interactions of the molecular species results in phase separation and formation of nanodomains[21-24] and, thus, randomness on a larger scale. While this might not be a critical issue for some properties such as wetting, for others like work function adjustment or chemical reactivity a more precise control is desirable, ideally down to molecular dimensions.

However, generating mixed SAMs with a well defined structure on a small scale is challenging as for thermodynamic reasons there is a driving force for either random mixing or phase separation, depending on whether the process is entropically or enthalpically driven. Therefore, unsurprisingly, the exploration of bottom-up strategies towards mixed monolayers with a well defined structure are very scarce.[25-28] Harnessing supramolecular recognition at the water/air interface locally ordered areas of guanidinium/orotate amphiphiles have been reported.[25] On an extended scale, mixed ordered thiol SAMs were prepared using sacrificial templates involving a two-dimensional supramolecular network[26] or an array of metal oxide nanoislands generated by

[a] EaStCHEM School of Chemistry, University of St Andrews, North Haugh, St Andrews KY16 9ST, United Kingdom, E-mail: mb45@st-andrews.ac.uk Fax: +44 1334 463808; Tel: +44 1334 463800
[b] Angewandte Physikalische Chemie, Universität Heidelberg, Im Neuenheimer Feld 253, 69120 Heidelberg, Germany

† Present addresses: (H.L.) Max Planck Institute for Polymer Research, Ackermannweg 10, 55128 Mainz, Germany.
(H.A.) Royal Society of Chemistry, Thomas Graham House, Science Park, Milton Road, Cambridge, CB4 0WF.

†The research data supporting this publication can be accessed at https://doi.org/10.17630/ d9f8a3cf-c46e-4d16-857a-1303a53cfc0b

substrate controlled organization.[27,28] Demonstrating the feasibility of regular structures with features 1-2 nm wide [26] the experiments also revealed the stringent requirements of controlling displacement and diffusion at such a small length scale. Using a temporary template necessarily involves a sequential process and it is obvious that diffusion plays a role upon removal of the template. However, even in more or less dense alkanethiol monolayers diffusion is an issue. [29]

While interactions between molecules and molecule-substrate have been identified as important parameters determining the structure of mixed SAMs, the influence of molecular geometry has hardly been explored. Studies on mixed SAMs, overwhelmingly performed with thiols,[1,30-32] have employed molecules based on chain-like alkanes,[23,29] more rigid rod-type aromatic systems,[33,34] combinations of aromatic/aliphatic molecules,[35,36] and alicyclic ring or small cage molecules.[37-39]

The work presented below is a step along the exploration of the influence of molecular geometry on the assembly of mixed layers. Instead of thiols a combination of carboxylic acids was studied, namely an aromatic carboxylic acid (H3BTB) and a cage-type aliphatic carboxylic acid (AdCA, for structures see Fig. 1). The choice of carboxylic acids is motivated by recent studies which have shown that aromatic carboxylic acids (ArCAs) can form highly crystalline layers of upright standing molecules on coordinating metals[40-45] metal oxides,[46,47] and even inert substrates such as Au.[48] Silver, prepared as an epitaxial bilayer on Au(111) by underpotential deposition (UPD), emerged as a particularly suitable substrate from recent studies. A small corrugation of the molecule-substrate interaction potential allowing for flexibility in the adsorption site, together with a moderately strong coordination bonding of carboxylate to Ag, makes intermolecular interactions the structure determining factors in carboxylic acid based SAMs.[41] Compared to thiols where the molecule-substrate bond exerts a decisive influence on the SAM structure,[49] this facilitates the design of SAMs based on the architecture of the molecular backbone. This combines favourably with the large variety of available aromatic carboxylic acids (ArCAs) which constitute essential building blocks of supramolecular assemblies both in solution and at interfaces.[50,51]

The particular choice of molecules, H3BTB and AdCA, is motivated by the specific structural features of the H3BTB monolayer. Whereas surface assembly of AdCA has, to the best of our knowledge, not been studied so far, our preceding investigations had established that, on Ag, H3BTB assembles to highly crystalline SAMs consisting of parallel rows of upright standing molecules.[52] Importantly, owing to their Y-shaped geometry and monopodal anchoring to the substrate, the SAM features an open structure as illustrated by the model in Fig. 1. In this way nanotunnels are formed of dimensions which should allow accomodation of smaller molecules such as AdCA, chosen as an illustrative example. This way H3BTB SAMs can be expected to template the arrangement of a second species, thus, representing an example to generate binary SAMs with order defined on the molecular length scale. Given the differences between H3BTB and AdCA as regards geometry, size, and intermolecular interactions, we were interested in elucidating the thermodynamic and kinetic factors of film formation and how these are affected by the preparation protocol, i.e., assembled in a sequential fashion or by coadsorption.

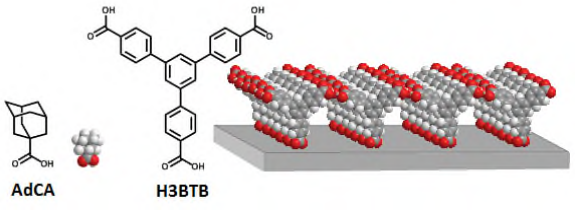

Fig. 1. Chemical structures of 1,3,5-benzenetribenzoic acid (H3BTB) and adamantanecarboxylic acid (AdCA) and structural model of an H3BTB SAM on Ag(111).

Results

STM: For reference, images of the monocomponent SAMs at larger scale and molecular resolution are presented in Fig. 2a-d. As detailed previously,[52] the H3BTB layer is characterized by domains of straight rows with intermolecular intrarow and interrow distances of 3.9 Å and 15.7 Å, respectively. Intrarow π-stacking, interrow H-bonding on either side of the rows by COOH moieties, and coordinative bonding of the molecules to the substrate via carboxylate result in the open structure shown in Fig. 1. AdCA also forms a highly crystalline SAM but, in contrast to the highly anisotropic structure of the H3BTB monolayer, molecules are hexagonally packed as seen from the molecular resolution image (Fig. 2d) and the Fourier transform of a domain (inset). A nearest neighbour distance of 6.2 Å results in an orientation off the high symmetry axes of the Ag(111) surface and, thus, the occurrence of rotated domains as seen in Fig. 2d. In both AdCA images molecule sized depressions are discernible, some of them encircled or marked by arrows. While their origin is not clear at present, the internal structure seen in the high resolution image of Fig. 2d suggests that these are not missing molecules but, reminiscent of point defects reported for C_{60} on Au(111),[53] might arise from defects in the substrate and/or a different electronic coupling of the molecule to the substrate. We consider trapped impurities a less likely explanation as these defects did not exhibit systematic variations with immersion time. For strongly adsorbing impurities an increase in their density with adsorption time would be observed, whereas weaker adsorbing species would be displaced by adamantane carboxylic acid.

Samples of bicomponent SAMs prepared by coadsorption under identical conditions, i.e., 65°C and 10 min immersion time, are presented in Fig. 2e-h. The influence of AdCA on the packing of H3BTB is obvious. Even though H3BTB still forms rows these are now rather wiggly with frequent substantial bends. Furthermore, the varying separation between rows can now also be as small as 1.1-1.2 nm, i.e., significantly smaller than in the highly ordered, pure H3BTB SAM. This means that different ways of π-stacking must be present including configurations with a more staggered arrangement. Even

though there is significant disorder, the presence of rows and their still largely parallel arrangement over significant distances evidence that interrow hydrogen bonding and π-stacking still prevail over interactions between AdCA and H3BTB. This suggests that AdCA molecules represent a kinetic barrier for H3BTB to maximize interactions by ordering. Looking at the changes upon variation of the H3BTB/AdCA ratio, the dispersion of AdCA in H3BTB is rather uniform over a wide range of compositions. There is no indication of phase separation and only at a large excess of AdCA larger areas of this component appear. We will return to this point later in the discussion.

Looking at the 1:99 sample in more detail, regions of low H3BTB concentration are discernible (encircled area in Fig. 2f) where the molecules arrange in filaments consisting of stacks of short rows instead of a small number of longer rows running along the filament. This suggests that the COOH interactions are more effective than π-π ones.

Studying the details of the mixed SAMs, a point worth mentioning is the quality of imaging. For the pure layers molecular resolution as shown in Fig. 2b and d can be rather easily obtained. In the mixed layer this is significantly more difficult as the well defined packing of the H3BTB is lost and distances are not as clearly defined anymore. Fig. 2h, which shows the H3BTB rows at high resolution in 3D representation, gives an impression of the reduced regularity. The molecules can be identified as small protrusions which exhibit varying distances between each other.

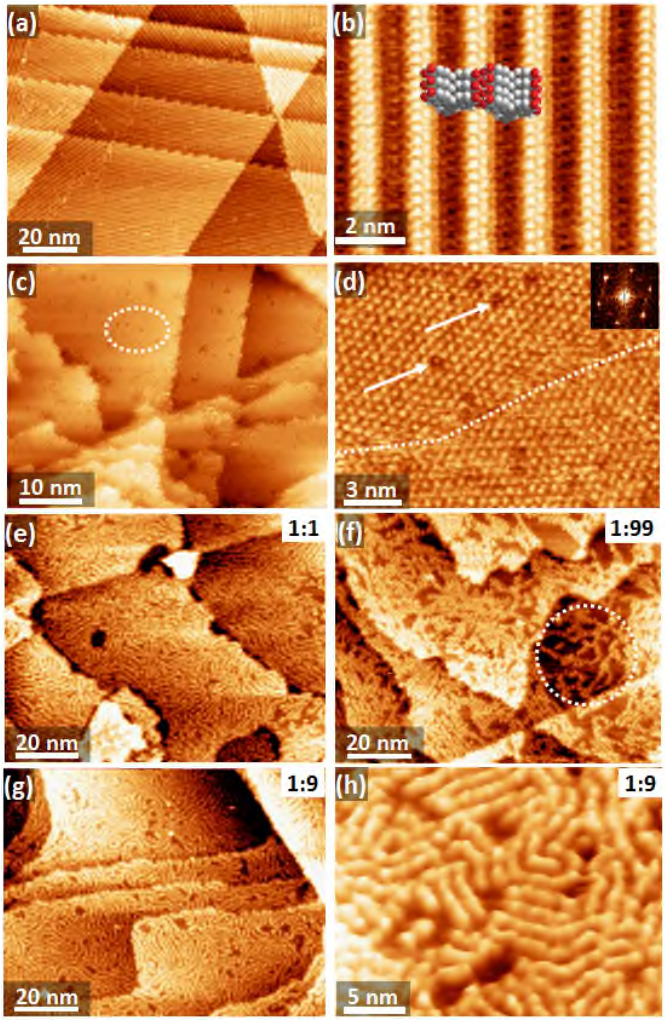

Fig. 2 STM images of H3BTB and AdCA assembled onto UPD-Ag separately or by coadsorption. a,b) pure H3BTB and c,d) pure AdCA layers at low and molecular resolution. Samples were prepared at 338 K by immersion in the respective solutions for 15 min (H3BTB) and 40 min (AdCA). Packing of molecules in H3BTB SAM is indicated by model in (b). Encircled area in (c) marks single molecule sized depressions in AdCA layer. Dashed line and arrows in (d) mark domain boundary and defects. Inset in (d) shows Fourier transform of upper domain. (e)-(g) Images of binary SAMs prepared from solutions with different H3BTB:AdCA ratios as indicated. (h) High magnification image of mixed SAM in 3D representation. Sum of H3BTB and AdCA concentrations in coadsorption experiments was 1 mM in all cases, i.e., H3BTB/AdCA concentration ratios (in mM) were 0.5/0.5 (e), 0.01/0.99 (f), and 0.1/0.9 (g,h). Tunneling conditions U_{tip}/I: (a) -0.4 V/1.5 pA, (b) -0.4 V/5 pA, (c) 0.5 V/10 pA, (d) 0.3 V/10 pA, (e) 0.65V/ 5 pA, (f) 0.65V/ 1.5 pA, (g,h) -0.65V/ 1.5 pA.

Turning to sequential adsorption, Fig. 3 summarizes results where AdCA SAMs were immersed into an H3BTB solution for different times. After a rather short immersion time of 2 min (Fig. 3a) filaments and islands of H3BTB molecules are observed which arise from insertion and exchange along domain boundaries and, to much lesser extent, inside AdCA domains. Interestingly, as in the coadsorption experiments the narrow filaments consist of an assembly of very short rows of H3BTB molecules aligned more or less perpendicular to the filament direction and not of extended rows running parallel to the chain. Again, this suggests that the formation of the chains is mediated by intermolecular interactions via the carboxylic acid groups and not by interaction of the π-systems

which would favour formation of rows. We explain this by the Y-shape of the H3BTB molecules. As illustrated by the model shown in Fig. 3a, the monopodal anchoring of the H3BTB molecule allows for intermolecular interactions via H-bonding of the COOH groups even if mixed with the shorter AdCA molecules. In contrast, for π-interactions to play a significant role, the H3BTB molecules have to be in close proximity. Since this is impeded by the AdCA molecules, stacking of H3BTB via π-interactions is less likely and, thus, row formation lags behind and requires longer immersion times as documented by Fig. 3c. In this context it is noted that further growth in width of the H3BTB chains becomes very slow indicating that, even at the elevated temperature employed here, a well packed AdCA layer is rather robust against displacement by H3BTB. This is also corroborated by the evolution of the H3BTB islands which do not increase markedly in size.

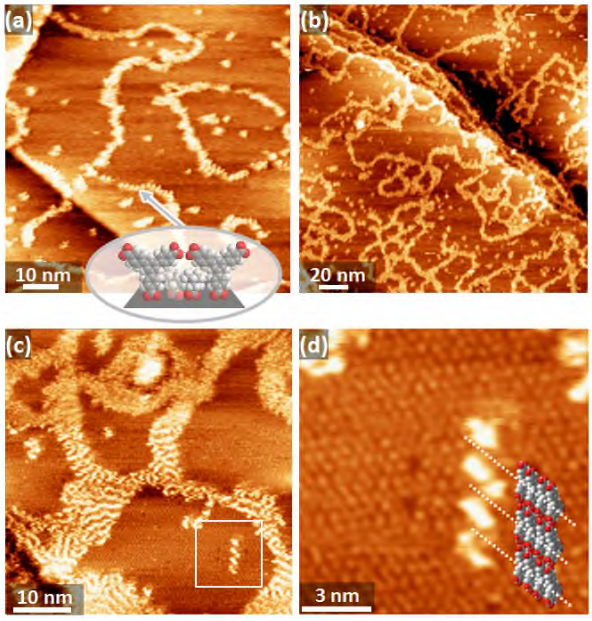

Fig. 3 STM images of a mixed AdCA/H3BTB layer on UPD-Ag prepared by exposing an AdCA SAM to a 1 mM H3BTB solution for 2 min (a), 10 min (b), and 12 min (c) at 338 K. Model in (a) illustrates the arrangement of H3BTB molecules along domain boundaries. (d) Close-up of area marked by white square in (c) which shows the AdCA matrix at molecular resolution and an agglomeration of short rows of H3BTB together with a model of the latter consisting of staggered H3BTB molecules. Tunneling conditions U_{tip}/I: (a) -0.4 V/5pA, (b-d) 0.7 V/1.5 pA.

Similar to the coadsorption experiments, AdCA prevents formation of straight H3BTB rows. A closer look at distances between rows reveals that these can be closer than the 15.7 Å of the highly crystalline layer. This is illustrated by the short segments framed in Fig. 3c and displayed at higher magnification in Fig. 3d which also shows the matrix of AdCA molecules at molecular resolution. The shape of the H3BTB features suggests stacks of a few molecules as indicated by the structural model in Fig. 3d. The separation of these short segments is in the range of 11.5-13.5 Å which is smaller than the 15.7 Å of the pure H3BTB layer and requires a staggered packing of the H3BTB molecules as indicated in the model. It is not clear at present what the factors are enforcing such a packing which is different from that found in a pure H3BTB SAM.

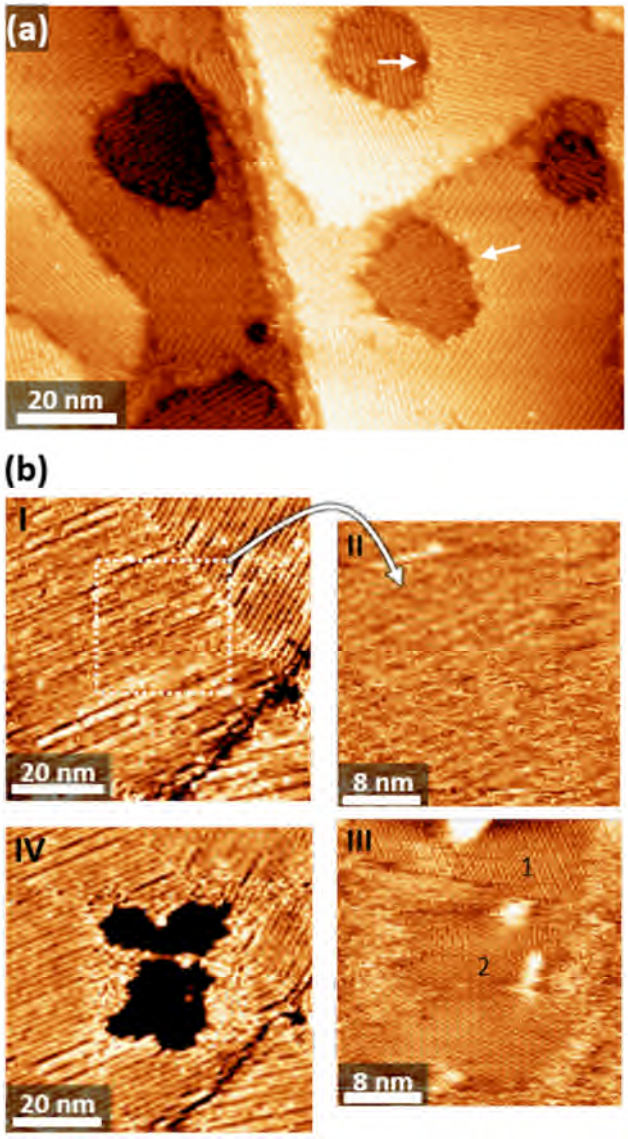

Fig. 4 (a) STM image of an H3BTB SAM on UPD-Ag after exposure to a solution of 1 mM AdCA at 338 K for 10 min. Arrows mark some of the small defect islands in the H3BTB SAM. (b) A SAM as depicted in (a) modified by STM scanning. The series of images shows the SAM before modification (I), at different stages during repeated scanning of the area marked by the dashed square under modifying conditions (II/III, 1st scan/6th scan), and after modification (IV) under the initial imaging conditions. Numbers in image III label differently orientated AdCA domains. Tunneling conditions U_{tip}/I: (a) 0.68 V/1.5 pA, (b) -0.4 V/5 pA (imaging) and 0.65 V/50 pA (modification).

Both coadsorption of AdCA/H3BTB and sequential adsorption of H3BTB after AdCA yield H3BTB in a poorly ordered state. In this situation we have not seen much potential in exploring longer immersion times for these preparation protocols but focused on the inversion of the sequence by exposure of a highly ordered layer of H3BTB to AdCA, which seemed the more interesting case, given the high crystallinity and open structure of an H3BTB SAM. As evidenced by the STM image shown in Fig. 4a, the H3BTB layer appears to be unaffected when exposed to AdCA. The characteristic row structure of the

native layer (see Fig. 2a) is maintained and no changes in the interrow distance is noticeable. At most, small defect spots appear (some of them marked by arrows in Fig. 4a). While this, obviously, demonstrates the stability of the H3BTB layer against displacement by AdCA, it is not clear whether AdCA is only adsorbed at defects or can intercalate into the nanotunnels of the H3BTB SAM. In the latter case, direct microscopic evidence of the presence of AdCA molecules would require selective removal of H3BTB. By serendipity we found conditions for such a removal which involve both a positive tip bias and a moderate increase in current. The underlying mechanism is not clear at present and further investigation has to clarify how much electrostatic and/or mechanical forces contribute. Following a protocol which comprises imaging of an area under non-modifying conditions (Fig. 4b, image I), several scans (typically 5-10) of a zoomed-in area under modifying conditions (II,III) and returning to the original image size and scanning parameters reveals the presence of AdCA.

In Fig. 4b-II, which shows the first image under modifying conditions, the row structure is still weakly discernible. This changes upon continuous scanning of the area. First, no features are resolved as images appear fuzzy which is interpreted as H3BTB molecules being removed and dragged along the surface by the STM tip. However, after a few scans the resolution improves locally, revealing small patches where the characteristic hexagonal packing of an ordered AdCA layer structure is resolved. Areas of molecular resolution further extend in subsequent scans until the fuzzy region is limited to the edges of the images as illustrated in Fig. 4b-III which represent the 6th scan. Zooming out (Fig. 4b-IV), the change in the modification area is evident whereas the row structure of the surrounding H3BTB SAM is unaffected. In the example shown, the area where H3BTB has been removed is partitioned into two sections which correspond to different domains of AdCA as inferred from (Fig. 4b-III). An obvious conclusion from this experiment is that AdCA intercalates in the tunnels of the H3BTB SAM. However, there are some caveats. One is that the AdCA domains consist of densely packed molecules which cannot be formed if only AdCA molecules from the area are available where H3BTB has been removed. A dense packing needs additional AdCA molecules which raises the question of their origin. A possible explanation is that they come from the surrounding area of the intact binary SAM which in turn poses another question, that of the driving force of expulsion of AdCA from the H3BTB nanochannels. In principle, it is also conceivable that there is no intercalation and AdCA diffuses from islands such as the ones labelled by arrows in Fig. 4a along domain boundaries. Also in this case the driving force and underlying mechanism are unclear. To shed further light on this, information on the amount of adsorbed AdCA is required.

XPS: To estimate the extent of AdCA adsorption mixed H3BTB/AdCA SAMs were characterised by XPS using different photon energies of 350 eV, 580 eV (synchrotron) and 1486 eV (monochromatized Al Kα). Over this range of energies the electron escape depth varies substantially, thus, providing additional information on the composition of the mixed SAMs. We note that the exact values of the attenuation lengths for our films are not known, since they depend on the packing density, molecular geometry and size which vary substantially across the different layers. Nevertheless, the extent of the attenuation effects can be coarsely understood on the basis of the reference literature values for a densely packed alkanethiolate monolayers on Au(111), viz. 4-6 Å and 24 Å for the O 1s photoelectrons at photon energies of 580 and 1486 eV, respectively, and 4-7 Å, 11.3 Å, and 28 Å for the C 1s photoelectrons at photon energies of 350, 580 and 1486 eV, respectively.[54]

Figs. 5 and 6 compile the O 1s and C 1s spectra of a mixed SAM prepared by sequential exposure (H3BTB SAM exposed to AdCA) in comparison with a binary SAM prepared by coadsorption from a 1:9 H3BTB/AdCA ratio. A pure H3BTB layer, which has been described in detail previously,[52] is also included as reference.

The O 1s region is described by the three components characteristic of aromatic carboxylic acids SAMs,[41,43,52,55] namely the signal of the anchoring carboxylate group (~530.3 eV), and the carbonyl (~531.4 eV) and hydroxyl (~533 eV) signals of the COOH moieties. The spectra were all consistently fitted with these components, a linear background, and the ratio of the two COOH components set to the stoichiometric value of 1. Since the COO^- signal appears only as a weak shoulder in the 580 eV spectra, thus, making its binding energy an unreliable fitting parameter, the difference in binding energy between the COO^- and C=O signals was fixed to the values obtained from the respective 1486 eV spectra. There are only minor variations in peak position between the pure H3BTB layer and the mixed SAMs such as the separation of the COO^- and the C=O peaks which is slightly wider for the mixed SAMs (1.25-1.3 eV) compared to 1.1 eV for the pure H3BTB layer, possibly a result of variations in intermolecular interactions.

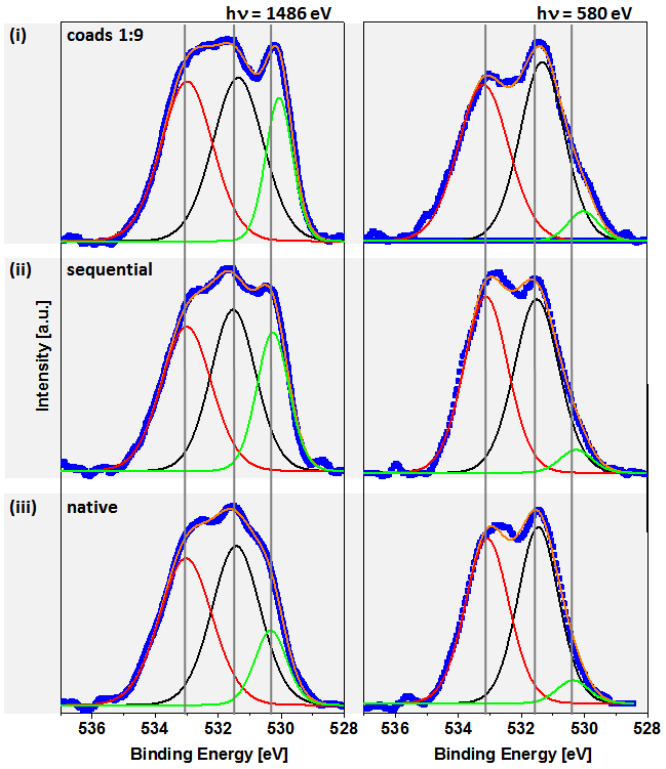

Fig. 5 O 1s XP spectra of bimolecular layers of H3BTB and AdCA on UPD-Ag substrates recorded with photon energies of 1486 eV (left panel) and 580 eV (right panel). Layers were prepared by coadsorption from a 1:9 mixture of H3BTB and AdCA in EtOH/H_2O (1:1) and by sequential adsorption (H3BTB SAM exposed to AdCA). Spectra of a pure H3BTB SAM are shown for comparison (iii). Blue squares represent the experimental data, and solid lines are the components (C-OH red, C=O black, COO^- green) and the joint envelope (orange) obtained from the fits.

In contrast, there are distinct changes in the signal intensities of the 1486 eV spectra going from the pure H3BTB SAM to the mixed layers. The smaller C=O/COO^- ratio of the mixed SAMs compared to the pure H3BTB monolayer (see Table 1) reflects a distinct increase in the contribution of the carboxylate signal, thus, indicating the presence of AdCA. Notably, the C=O/COO^- ratio is very similar for the sequential H3BTB-AdCA adsorption and coadsorption from the 1:9 mixture despite the very strikingly different film structures observed by STM (Figs. 2 and 4). We note that comparison of the spectra of the two samples requires some caution as a quantitative interpretation is limited due to uncertainties in decomposition of the O 1s signal. As discussed previously for SAMs of oligophenylenecarboxylic acids,[41] the native substrate is prepared electrochemically and, has a significant signal in the O 1s region originating from adsorbed OH and H_2O. These are displaced by the carboxylic acids and, therefore, represent not an issue for densely packed SAMs like the coadsorption sample or the AdCA SAM exposed to H3BTB. However, for H3BTB with its open structure a signal can come from residual OH/H_2O in the areas of the nanotunnels which are free of carboxylate. That signal will only disappear upon AdCA intercalation. Consequently, the background signal in the COOH region decreases whereas the COO^- signal increases upon AdCA adsorption. Due to the changing OH/H_2O background, the amount of AdCA derived from the C=O/COO^- signal ratio is overestimated and should be seen as an upper limit. Another factor is the increase in attenuation of the COO^- signal upon AdCA intercalation which affects the C=O/COO^- signal ratio oppositely. Neglecting these effects the result suggests that at least 1/3 of the carboxylate signal comes from AdCA, i.e., even in the case of the sequential H3BTB-AdCA adsorption where no obvious changes in the row structure of H3BTB are visible by STM. This substantial contribution of AdCA is far too large to be explained by the small defect islands such as the ones highlighted by arrows in Fig. 4a. Therefore, it has to be concluded that AdCA is intercalated in the nanotunnels of the H3BTB SAM, which also corroborates the interpretation of the STM experiments that, upon removal of H3BTB (Fig. 4b-III), areas of densely packed AdCA molecules are formed from intercalated AdCA molecules which bind coordinatively to the substrate. It is also noted that the substantial contribution of AdCA to the carboxylate signal is not consistent with the possibility that formation of areas of a dense AdCA SAM upon shaving comes from a reservoir of physisorbed, non-coordinated AdCA molecules.

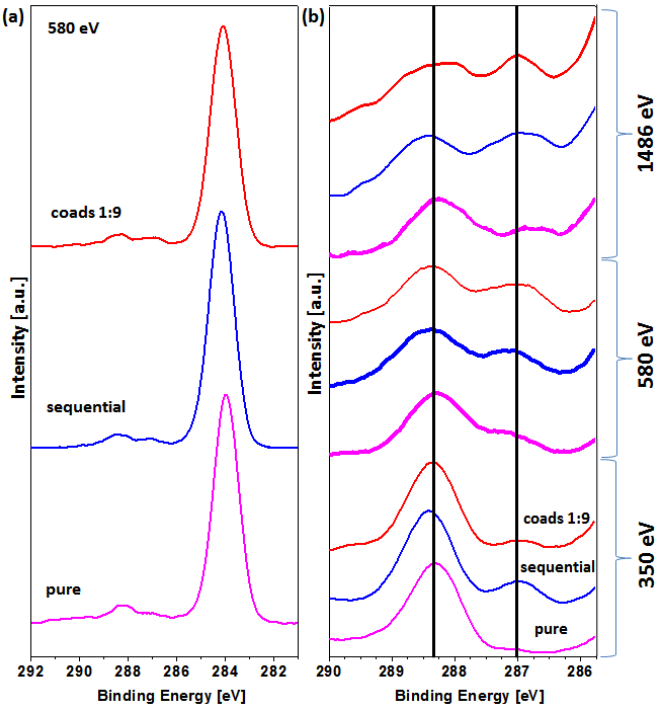

Fig. 6 C 1s XP spectra of pure H3BTB SAM (magenta curve) and mixed layers of H3BTB and AdCA (blue: sequential adsorption, red: coadsorption 1:9) on UPD-Ag substrates recorded for photon energies of 1486 eV, 580 eV, and 350 eV. (a) 580 eV spectra of extended C 1s region showing a main peak at ~284.2 eV and two weak components characteristic of COO^- (~287 eV) and COOH (~288.5 eV). (b) COO^- and COOH signals for different SAMs and different photon energies. Preparation conditions as described in Fig. 5.

Looking at the corresponding 580 eV spectra, the main difference compared to the 1486 eV data is the significantly larger C=O/COO^- ratio due to the stronger attenuation of the signal of the carboxylate moiety located at the buried SAM-substrate interface. Noting that, due to the small magnitude of

the COO^- signal, the error margins for this component are substantial and, therefore, the intensities should be considered as an upper limit, the attenuation appears to be rather similar for both the pure H3BTB layer and the mixed SAMs. This reflects two compensating effects related to the adsorption of AdCA. On the one hand, it increases the number of carboxylate moieties but, on the other hand, also increases the material density in the layer, thus, causing a stronger attenuation of the COO^- photoelectrons.

The C 1s spectra, shown over the entire region for a photon energy of 580 eV in Fig. 6a and in the region of the COO^- (287 eV) and COOH signals (288.5 eV) for all three photon energies in Fig. 6b, also reflect the composition of the SAMs. Whereas the dominating peak at ~284.2 eV, containing the signal from the phenyl rings of H3BTB and the adamantane cage, is common to all systems and does not vary significantly, the $COOH/COO^-$ region detailed in Fig. 6b evidence the contribution of AdCA. At all three photon energies there is a substantial increase of the carboxylate signal relative to the COOH one due to AdCA. Similar to the O 1s spectra, the SAMs prepared by coadsorption and sequential adsorption yield similar intensity ratios (for values see Table 1). There is a continuous increase of the COO^- signal with increasing photon energy as a consequence of the progressively weaker attenuation of the photoelectrons. Like the O 1s spectra, the C 1s spectra of the two mixed SAMs are very similar for a given photon energy. The $COOH/COO^-$ ratio of 1 for the 1486 eV spectra is substantially larger than the value for the pure H3BTB, thus further evidencing the substantial intercalation of AdCA upon the sequential preparation.

Table 1. Intensity ratios of the characteristic XPS signals for the H3BTB SAMs, pure and mixed with AdCA. Error margins of the values are about ±10%.

	Photon energy [eV]	O 1s C=O/COO^-	C 1s COOH/COO^-
H3BTB	1486	3	2.6
	580	9.9	2.2
	350	--	10.6
H3BTB/AdCA 1:9 coadsorbed	1486	2.1	1
	580	8.8	1.5
	350	--	3.5
H3BTB → AdCA sequential	1486	2.0	1.0
	580	10.5	1.5
	350	--	3.0

NEXAFS: Since, as seen from the comparison of the STM images (Figs. 2 to 4), the protocol for the preparation of mixed H3BTB/AdCA layers has a pronounced influence on the coverage and order in the arrangement of the H3BTB molecules, the samples were characterized by NEXAFS spectroscopy, in order to complement the XPS measurements and assess differences in the orientation of H3BTB between the pure and differently prepared mixed SAMs. The results are compiled in Fig. 7.

The 55° spectra (top panel) which are insensitive to orientational effects are of similar shape for all samples and characterised by the sharp π*-resonances from the electronic transitions involving aromatic rings (π^*_{Ph}, 285 eV) and carboxylic acid groups (π^*_{COOH}, 288.5 eV), the latter comprising both the free protonated moieties and the carboxylate anchor groups. The most obvious difference between the spectra is the intensity of the π^*_{Ph}-resonance which is clearly lower for the mixed SAMs compared to the pure H3BTB monolayer. Noting that the spectra are normalised to the height of the carbon edge, which is determined by the sum of aliphatic (AdCA) and aromatic (H3BTB) carbon whereas the π^*_{Ph}-signal only comes from H3BTB, the decrease in intensity of the latter, again, evidences the presence of AdCA. Also, the very similar intensity of the π^*_{Ph}-signal for the mixed SAMs prepared by coadsorption and sequential adsorption indicates that the amounts of AdCA in both layers are comparable. This further supports the conclusions drawn above that the H3BTB SAM can intercalate significant amounts of AdCA in its nanotunnels.

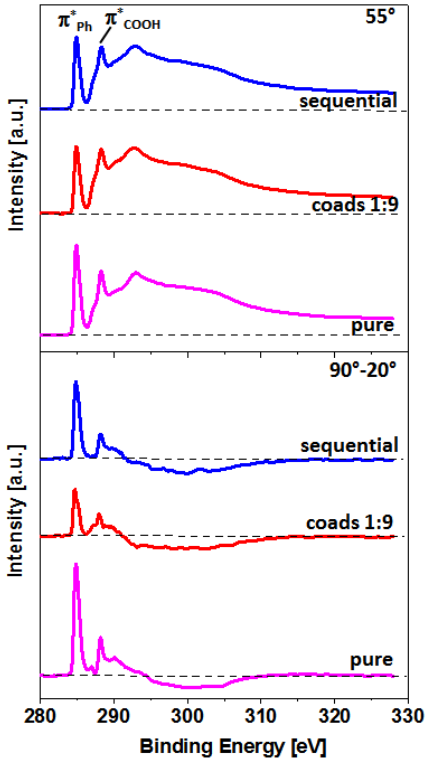

Fig. 7 C K-edge NEXAFS spectra of SAMs of H3BTB only (magenta curve) and mixed with AdCA (red: coadsorption 1:9, blue: AdCA-after-H3BTB sequential adsorption). Top panel: spectra acquired at an X-ray incidence angle of 55°. Bottom panel: Differences of spectra acquired at X-ray incidence angles of 20° and 90° with respect to the surface. The most prominent π*-resonances are labelled. Dashed lines correspond to zero.

The difference spectra (bottom panel) which contain information on the molecular orientation also show substantial variations across the systems. The dichroism of the π^*_{Ph} resonance is largest for the pure H3BTB (magenta curve), indicating a smaller average tilt angle of the molecules

compared to the binary SAMs. The quantitative evaluation yields values of 66.5° for pure H3BTB, 64° for sequential adsorption, and 61° for coadsorption. These are small but significant differences and while the absolute error of NEXAFS-derived tilt angle values is generally believed to be about ±3°, the values obtained consistently with the same experimental setup can be compared to one another with an error of about ±1° as verified by acquisition of several data sets. Since the measured values represent an average from transitions in all aromatic rings of H3BTB, changes do not necessarily mean just a different molecular orientation. An additional factor influencing the value is the distribution of orientations with a larger distribution of tilt angles moving the average value towards the isotropic value of 54.7°. Applied to the case of H3BTB, the decrease in the average tilt angle going from the highly crystalline H3BTB SAM (see Fig. 2a and b) to a much less ordered H3BTB/AdCA coadsorption layer (Fig. 2e-h) is interpreted to arise from the difference between a uniform orientation of essentially coplanar H3BTB molecules and less uniformly orientated molecules with, furthermore, an increased number of conformations afforded by the less dense packing. An interesting case is the SAM prepared by sequential adsorption as STM (Fig. 4a) does not reveal any obvious difference to the pure H3BTB layer. Nevertheless, there is a small but distinct change in the average tilt angle to the smaller value. Given the dense packing of the H3BTB molecules it seems difficult to explain this by a uniform reorientation which would also raise the question what the driving force were. Instead it seems more plausible that the intercalation of AdCA causes conformational changes in the H3BTB molecules, i.e., an increase in the distribution of orientations of the transition dipole moments by changes in the twist angles between the individual aromatic rings.

Discussion

The pronounced intermolecular interactions of H3BTB involving both π–π interactions and H-bonding between the COOH groups is a dominant feature in all mixed H3BTB/AdCA SAMs. Clearly favouring a row structure and partial alignment of rows it, nevertheless, allows for a substantial flexibility in the arrangements due to a manifold of configurations involving different conformations of the molecule (twist of individual rings), H-bonding motives, and stacking of the aromatic rings. The combination of the Y-shaped geometry of H3BTB with its monopodal adsorption mode favours intermolecular interactions of the COOH side groups over the interactions of the aromatic rings when AdCA is present and these are rather insensitive to the presence of the smaller AdCA molecules as evidenced by the samples prepared by coadsorption (Fig. 2). The film morphology and, therefore, the amount and distribution of H3BTB, remains very similar over a wide range of H3BTB/AdCA concentration ratios. This is quite different from binary SAMs of aliphatic thiols where phase separation is particularly favoured if H-bonding is enabled between one type of molecule by amide groups.[56] However, it is similar to the case of mercaptophenylterpyridyl mixed with benzene thiol which also combines a larger Y-shaped molecule with a short one. Analysis of that system by XPS and ToF-SIMS revealed a very weak dependence of the mole fraction of the terpyridyl molecule on the solution composition (0.1-0.8).[7] In the present case, the limited influence of a significant excess of AdCA molecules indicates a much higher sticking probability of H3BTB which is explained by the combination of statistics and differences in intermolecular interactions. The former refers to the statistical weight of a configuration where the carboxyl group is facing the substrate prior to adsorption of the molecule by coordination bonding. Since H3BTB has three COOH groups whereas AdCA has only one, the sticking probability is higher for H3BTB. The latter refers to different types of interactions, weak van der Waals interactions for AdCA, and stronger H-bonding and π-π interactions for H3BTB. In combination with the difference in size of the molecules, H3BTB exhibits an interaction volume significantly larger than AdCA.

Owing to the significant differences in size, geometry, and intermolecular interactions, a very asymmetric behaviour is observed with respect to the deposition sequence. Similar to other systems consisting of mixed alkane thiols,[57] or an alkane mixed with biphenyl thiols[22,36] insertion of H3BTB into an AdCA SAM starts at defects and, to some degree, occurs also within islands as e.g. described for the dodecane thiol/biphenylbutane thiol system.[36] Interestingly, in the case of H3BTB there is a preference for insertion along the domain boundaries with the molecules interacting sideways via the COOH groups and slower progression into domains by stacking involving π–π interactions. Upon reversal of the sequence, the open geometry of the H3BTB SAM allows intercalation of AdCA without affecting the highly regular row structure of the host layer. We are not aware of other examples where an organized binary SAM involving upright standing molecules is formed without an additional templating such as a supramolecular network.[26] At best a random mixing at the molecular level can be achieved.[1,16,31]

The pronounced dependence of the SAM structures on the preparation protocol is also a reflection of kinetically vs thermodynamically controlled assembly. Coadsorption of the two molecules and sequential adsorption of H3BTB after AdCA are governed by kinetics whereas intercalation of AdCA into an H3BTB SAM is driven by minimization of the free energy. H3BTB forms more stable SAMs than AdCA due to the stronger intermolecular interactions but its Y-shape and monopodal adsorption geometry leave free adsorption sites in the nanotunnels. Intercalation of AdCA occupies those sites, and, therefore, minimizes the free energy of the system by maximising the density of molecule-substrate bonds. For the other two preparation protocols optimisation of the intermolecular interactions between H3BTB molecules is impeded by the simultaneous presence of AdCA which affects the mobility of H3BTB and its ability to assemble to well-ordered rows.

As regards the thermodynamics of the intercalated AdCA/H3BTB system there is another interesting aspect. Filling of the nanotunnels upon exposure of an H3BTB SAM to an

AdCA solution, as illustrated by the cartoon in Fig. 8a-c, is a spontaneous process, driven by the exothermic coordination bonding of AdCA to the substrate. In a simple geometric picture based on a space filling model and rigid packing of H3BTB molecules the space available in the nanotunnels should be sufficient to add AdCA corresponding to at least 1/3 of the number of H3BTB molecules. This is in the range derived from the XPS data and could be higher if some alterations in the stacking of the H3BTB molecules were possible, for example, by intrarow variations in the separation of the anchoring benzoic acid moieties. The extent to which AdCA is intercalated depends on the balance of different factors. One is the coordination bonding as driving force for maximising the filling of the nanotunnels with AdCA. It is opposed by forces arising from endergonic contributions. Besides repulsive intermolecular interactions among AdCA, and between AdCA and H3BTB molecules, this also includes structural distortion of the H3BTB layer involving enthalpic strain and a decrease in entropy due to a reduced conformational space of the H3BTB molecules. The NEXAFS difference spectra (Fig. 7), reflecting small orientational changes in the H3BTB layer upon AdCA intercalation, corroborate this.

When the balance is perturbed, as done in the shaving experiments (Fig. 4b) where H3BTB is locally removed, the system evolves towards a new equilibrium characterized by a crystalline AdCA SAM in areas void of H3BTB molecules (Fig. 8f). At first glance this seems surprising since a submonolayer coverage of AdCA should yield an incomplete and disordered AdCA layer as illustrated in Fig. 8d-e. For clarity showing the idealized situation where H3BTB is instantaneously removed and then followed by spreading of AdCA, the two steps, in fact, proceed concurrently. Noting that the sequence from (d) to (f) is too fast to be resolved in the experiment, the crucial point is that a crystalline SAM of densely packed AdCA molecules, as observed by STM (Fig. 4b-III) and illustrated in Fig. 8f, can only be formed in the H3BTB-free areas if there is supply of additional AdCA from the surrounding, "pristine" area, with the nanotunnels serving as reservoir. Energetically, the removal of H3BTB molecules creates alternative adsorption sites which can be occupied by AdCA with the energy gain provided by both the formation of ordered AdCA SAM and a reduction of strain in the AdCA providing nanotunnels. In other words the creation of an H3BTB-free area shifts the balance of forces such that, at a fixed overall AdCA coverage, the deformation of the H3BTB layer is reduced and exposed areas of the substrate are covered by a dense layer of AdCA molecules.

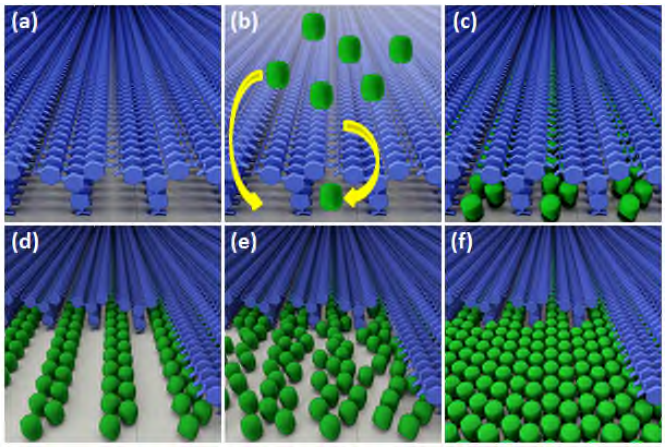

Fig. 8 Illustration of AdCA intercalation into a SAM of H3BTB (a-c) and subsequent aggregation of AdCA SAM in areas where H3BTB was mechanically removed (d-f). H3BTB in blue, AdCA in green. For details see text.

Conclusions

Formation of a highly regular binary SAM where one of the components (H3BTB) acts as template for the second one (AdCA) contrasts the behaviour of other two component SAMs for which, in general, disordered mixed or phase separated layers, or random partial displacement is observed, depending on preparation protocol and molecular composition. It is a consequence of the Y-shape of H3BTB, its monopodal adsorption geometry, and interaction between the terminal COOH groups which gives rise to an open SAM structure featuring nanotunnels. These, in turn, allow for intercalation of a second species in a structurally well-defined manner.

While the intercalated molecules are hidden from the outer SAM interface and, thus, do not allow its direct chemical functionalisation, other properties should be affected. One is the work function which is anticipated to be influenced by intercalation of molecules with varying dipole moment, similar to studies where dipolar groups are incorporated into the backbone of SAM forming molecules.[17,58] Another aspect is the possibility to combine aromatic and aliphatic species in a well defined way. This is an interesting feature to explore towards the formation of carbon nanomembranes by electron-induced crosslinking as the two types show opposite resist behaviour, negative for aromatic, positive for aliphatic SAMs.[59,60]

Conceptionally, it will be of interest to develop this type of SAM templating further beyond ongoing experiments investigating changes in the size of nanotunnels by using larger homologues and derivatives of H3BTB. Instead of using planar molecules like H3BTB, polyfunctional aromatic carboxylic acids exhibiting a three dimensional structure should allow the design of even more open structures featuring molecule sized pores, thus, offering the prospect of templating another SAM species in an ultraprecise way down to the level of isolated molecules.

Experimental

Substrate and Monolayer Preparation

Substrates were prepared by electrodepositing a bilayer of Ag onto Au films (300 nm layer of Au(111) on mica, Georg-Albert PVD, Silz, Germany) in the underpotential region as previously described.[52] The Au substrates were flame-annealed prior to the deposition, using a Bunsen burner running with natural gas. After the underpotential deposition (UPD) of the Ag bilayer, substrates were immersed in the respective solutions of either one of the carboxylic acids or a mixture of both. The substances were recrystallized from EtOH and 1 mM stock solutions were used. The solvent was a 1:1 water (Millipore)/ethanol (AnalaR Normapur) mixture. For mixed solutions the total concentration was kept at 1 mM at H3BTB ratios as given in the text. Noting that the quality of the single component layers is not noticeably affected by the immersion time if sufficiently long to ensure complete layer formation, exact immersion times are stated throughout the text. Samples were prepared at 338 K, chosen to be still well below the boiling point of ethanol but promoting larger domain size for the single component SAMs and accelerating processes such as exchange in mixed SAMs compared to room temperature. After immersion, samples were always rinsed with ethanol and dried in a stream of nitrogen.

Characterization

Scanning tunneling microscopy (Molecular Imaging PicoSTM, Picoscan Version 5.3.3 software) in ambient environment conditions was used for structural characterization. Tips were manually cut from a 0.25 mm diameter Pt/Ir wire (80:20, hard-tempered, Advent Research Material Ltd.). Images were acquired in constant current mode with tunneling currents (IT) and tip bias (V) in the range of 1-100 pA and ±0.200-0.800 V. Images were evaluated using WSxM software.[61]

XPS and NEXAFS: In-house XPS was performed with a Scienta 300 spectrometer and a monochromatized Al Kα source (1486.6 eV). Spectra were collected at a pass energy of 150 eV, the width of the Au $4f_{7/2}$ line was about 0.9 eV.

High resolution XPS and NEXAFS spectroscopy measurements were carried at the HE-SGM beamline (bending magnet) of the synchrotron storage ring BESSY II in Berlin.

XPS spectra were measured with a Scienta R3000 electron energy analyzer, in normal emission geometry. The energy resolution was ~0.3 eV and ~0.5 eV at photon energy of 350 and 580 eV, respectively. The binding energy scale was referenced to the Au $4f_{7/2}$ peak at a BE of 84.0 eV.[62] Spectra were fitted employing a Gaussian/Lorentzian product function (GL30) and a linear background using Casa-XPS software.

The NEXAFS spectroscopy measurements were made using a partial electron yield detector. The spectra were collected at the carbon K-edge with a retarding voltage of −150 V. Linear polarized X-ray light with a polarization factor of ~90% was used. The energy resolution was ~0.3 eV. The incident angle of the X-ray light was varied from 90° (E-vector in the surface plane) to 20° (E-vector nearly normal to the surface plane) in steps of 10-20°, to monitor orientational order of the aromatic carboxylic acid molecules in the SAMs. This approach is based on the linear dichroism in X-ray absorption, i.e., the strong dependence of the cross-section of the resonant photo-excitation process on the orientation of the electric field vector of the linearly polarized light with respect to the molecular orbital of interest.[63]

The raw NEXAFS spectra were normalized to the incident photon flux by division by a spectrum of a clean, freshly sputtered gold sample. Afterwards, the spectra were reduced to standard form by subtracting a linear pre-edge background and normalizing to the unity jump edge in the far post-edge range. The energy scale was referenced to the most intense π^* resonance of highly oriented pyrolytic graphite at 285.38 eV.[64]

Conflicts of interest

There are no conflicts to declare.

Acknowledgements

Support by the Leverhulme Trust (RGP-2013-177) and EPSRC via doctoral training grants (R.O.d.l.M., H. A.) and the EPSRC Centre for Doctoral Training in Critical Resource Catalysis (CRITICAT) (PhD studentship to K.T.) is gratefully acknowledged. A.A. and M.Z. thank the Helmholtz Zentrum Berlin for the allocation of synchrotron radiation beamtime at BESSY II and A. Nefedov and Ch. Wöll for the technical cooperation there. A.A. acknowledges the financial support by the DAAD-Aceh Scholarship of Excellence.

Notes and references

1. M. D. Marquez, O. Zenasni, A. C. Jamison and T. R. Lee, *Langmuir*, 2017, **33**, 8839-8855.
2. C. D. Bain and G. M. Whitesides, *J. Am. Chem. Soc.*, 1988, **110**, 6560-6561.
3. P. E. Laibinis, R. G. Nuzzo and G. M. Whitesides, *J. Phys. Chem.*, 1992, **96**, 5097-5105.
4. J. P. Folkers, P. E. Laibinis and G. M. Whitesides, *Langmuir*, 1992, **8**, 1330-1341.
5. M. Zwahlen, W. R. Caseri and G. Hahner, *Z. Physikal. Chem.*, 2008, **222**, 823-832.
6. S. Morgenthaler, C. Zink and N. D. Spencer, *Soft Matter*, 2008, **4**, 419-434.
7. A. Auditore, N. Tuccitto, G. Marzanni, S. Quici, F. Puntoriero, S. Campagna and A. Licciardello, *Chem. Commun.*, 2003, DOI: 10.1039/B305484E, 2494-2495.
8. C. Musumeci, G. Zappalà, N. Martsinovich, E. Orgiu, S. Schuster, S. Quici, M. Zharnikov, A. Troisi, A. Licciardello and P. Samorì, *Adv. Mater.*, 2014, **26**, 1688-1693.
9. H. Tokuhisa and R. M. Crooks, *Langmuir*, 1997, **13**, 5608-5612.
10. D. T. Valley, M. Onstott, S. Malyk and A. V. Benderskii, *Langmuir*, 2013, **29**, 11623-11631.
11. T. Moldt, D. Brete, D. Przyrembel, S. Das, J. R. Goldman, P. K. Kundu, C. Gahl, R. Klajn and M. Weinelt, *Langmuir*, 2015, **31**, 1048-1057.

12. R. M. Mayall, M. Renaud-Young, E. Gawron, S. Luong, S. Creager and V. I. Birss, *Acs Sensors*, 2019, **4**, 143-151.
13. G. Liu, M. N. Paddon-Row and J. Justin Gooding, *Chem. Commun.*, 2008, , 3870-3872.
14. K. Y. Wu, S. Y. Yu and Y. T. Tao, *Langmuir*, 2009, **25**, 6232-6238.
15. J. Kim, Y. S. Rim, Y. S. Liu, A. C. Serino, J. C. Thomas, H. J. Chen, Y. Yang and P. S. Weiss, *Nano Lett.*, 2014, **14**, 2946-2951.
16. I. Hehn, S. Schuster, T. Wächter, T. Abu-Husein, A. Terfort, M. Zharnikov and E. Zojer, *J. Phys. Chem. Lett.*, 2016, **7**, 2994-3000.
17. E. Sauter, C. O. Gilbert, J. F. Morin, A. Terfort and M. Zharnikov, *J. Phys. Chem. C*, 2018, **122**, 19514-19523.
18. S. Watcharinyanon, E. Moons and L. S. O. Johansson, *J. Phys. Chem. C*, 2009, **113**, 1972-1979.
19. L. A. Bumm, J. J. Arnold, L. F. Charles, T. D. Dunbar, D. L. Allara and P. S. Weiss, *J. Am. Chem. Soc.*, 1999, **121**, 8017-8021.
20. S. Chen, L. Li, C. L. Boozer and S. Jiang, *Langmuir*, 2000, **16**, 9287-9293.
21. Y. Sato, R. Yamada, F. Mizutani and K. Uosaki, *Chem. Lett.*, 1997, DOI: 10.1246/cl.1997.987, 987-988.
22. D. M. Fitzgerald, E. K. Krisanda, C. G. Szypko and L. G. Avila-Bront, *Surf. Sci.*, 2017, **662**, 102-112.
23. R. K. Smith, S. M. Reed, P. A. Lewis, J. D. Monnell, R. S. Clegg, K. F. Kelly, L. A. Bumm, J. E. Hutchison and P. S. Weiss, *J. Phys. Chem. B*, 2001, **105**, 1119-1122.
24. S. J. Stranick, S. V. Atre, A. N. Parikh, M. C. Wood, D. L. Allara, N. Winograd and P. S. Weiss, *Nanotechnology*, 1996, **7**, 438-442.
25. Y. Oishi, Y. Torii, T. Kato, M. Kuramori, K. Suehiro, K. Ariga, K. Taguchi, A. Kamino, H. Koyano and T. Kunitake, *Langmuir*, 1997, **13**, 519-524.
26. C. Silien, M. T. Räisänen and M. Buck, *Small*, 2010, **6**, 391-394.
27. N. Battaglini, Z. Qin, P. Campiglio, V. Repain, C. Chacon, S. Rousset and P. Lang, *Langmuir*, 2012, **28**, 15095-15105.
28. R. Breitwieser, M. Marsault, V. Repain, J. Lagoute, C. Chacon, Y. Girard, S. Rousset, Z. Qin, N. Battaglini, S. Zrig and P. Lang, *J. Chem. Phys.*, 2013, **139**, 204703.
29. S. J. Stranick, A. N. Parikh, Y. T. Tao, D. L. Allara and P. S. Weiss, *The Journal of Physical Chemistry*, 1994, **98**, 7636-7646.
30. J. Z. Gao, F. S. Li and Q. M. Guo, *Langmuir*, 2013, **29**, 11082-11086.
31. Q. Ong, N. Nianias and F. Stellacci, *Epl*, 2017, **119**, 66001,66001-66007.
32. R. K. Smith, P. A. Lewis and P. S. Weiss, *Prog. Surf. Sci.*, 2004, **75**, 1-68.
33. T. D. Dunbar, M. T. Cygan, L. A. Bumm, G. S. McCarty, T. P. Burgin, W. A. Reinerth, L. Jones, J. J. Jackiw, J. M. Tour, P. S. Weiss and D. L. Allara, *J. Phys. Chem. B*, 2000, **104**, 4880-4893.
34. A. Ulman, *Acc. Chem. Res.*, 2001, **34**, 855-863.
35. M. C. R. Gonzalez, A. G. Orive, P. Carro, R. C. Salvarezza and A. H. Creus, *J. Phys. Chem. C*, 2014, **118**, 30013-30022.
36. B. Lüssem, L. Müller-Meskamp, S. Karthäuser, R. Waser, M. Homberger and U. Simon, *Langmuir*, 2006, **22**, 3021-3027.
37. J. N. Hohman, S. A. Claridge, M. Kim and P. S. Weiss, *Mater. Sci. Eng. R.*, 2010, **70**, 188-208.
38. H. M. Saavedra, C. M. Barbu, A. A. Dameron, T. J. Mullen, V. H. Crespi and P. S. Weiss, *J. Am. Chem. Soc.*, 2007, **129**, 10741-10746.
39. T. Sung, C. H. Lee, J. W. Han and J. Noh, *Bull. Korean Chem. Soc.*, 2017, **38**, 1381-1382.
40. H. Aitchison, R. Ortiz de la Morena, R. Peifer, S. Omar, H. Lu, S. M. Francis, M. Zharnikov, A. Grohmann and M. Buck, *Langmuir*, 2018, DOI: 10.1021/acs.langmuir.8b01734.
41. H. Aitchison, H. Lu, S. W. L. Hogan, H. Früchtl, I. Cebula, M. Zharnikov and M. Buck, *Langmuir*, 2016, **32**, 9397-9409.
42. H. Aitchison, H. Lu, M. Zharnikov and M. Buck, *J. Phys. Chem. C*, 2015, **119**, 14114-14125.
43. I. Cebula, H. Lu, M. Zharnikov and M. Buck, *Chem. Sci.*, 2013, **4**, 4455 - 4464.
44. C. Shen, I. Cebula, C. Brown, J. Zhao, M. Zharnikov and M. Buck, *Chem. Sci.*, 2012, **3**, 1858-1865.
45. I. Cebula, C. Shen and M. Buck, *Angew. Chem. Int. Ed.*, 2010, **49**, 6220-6223.
46. W. J. I. DeBenedetti and M. A. Hines, *J. Phys. Chem. C*, 2019, **123**, 8836-8842.
47. E. S. Skibinski, A. Q. Song, W. J. I. DeBenedetti, A. G. Ortoll-Bloch and M. A. Hines, *J. Phys. Chem. C*, 2016, **120**, 11581-11589.
48. K. N. Johnson, M. J. Hurlock, Q. Zhang, K. W. Hipps and U. Mazur, *Langmuir*, 2019, **35**, 5271-5280.
49. P. Cyganik, M. Buck, T. Strunskus, A. Shaporenko, J. D. E. T. Wilton-Ely, M. Zharnikov and C. Wöll, *J. Am. Chem. Soc.*, 2006, **128**, 13868-13878.
50. S. Furukawa, J. Reboul, S. Diring, K. Sumida and S. Kitagawa, *Chem. Soc. Rev.*, 2014, **43**, 5700-5734.
51. J. Liu and C. Wöll, *Chem. Soc. Rev.*, 2017, **46**, 5730-5770.
52. H. Aitchison, H. Lu, R. Ortiz de la Morena, I. Cebula, M. Zharnikov and M. Buck, *Phys. Chem. Chem. Phys.*, 2018, **20**, 2731-2740.
53. J. A. Gardener, G. A. D. Briggs and M. R. Castell, *Phys. Rev. B*, 2009, **80**.
54. C. L. A. Lamont and J. Wilkes, *Langmuir*, 1999, **15**, 2037-2042.
55. A. Dmitriev, H. Spillmann, S. Stepanow, T. Strunskus, C. Wöll, A. P. Seitsonen, M. Lingenfelder, N. Lin, J. V. Barth and K. Kern, *ChemPhysChem*, 2006, **7**, 2197-2204.
56. P. A. Lewis, R. K. Smith, K. F. Kelly, L. A. Bumm, S. M. Reed, R. S. Clegg, J. D. Gunderson, J. E. Hutchison and P. S. Weiss, *J. Phys. Chem. B*, 2001, **105**, 10630-10636.
57. Z. J. Donhauser, D. W. Price, J. M. Tour and P. S. Weiss, *J. Am. Chem. Soc.*, 2003, **125**, 11462-11463.
58. T. Abu-Husein, S. Schuster, D. A. Egger, M. Kind, T. Santowski, A. Wiesner, R. Chiechi, E. Zojer, A. Terfort and M. Zharnikov, *Adv. Funct. Mater.*, 2015, **25**, 3943-3957.
59. M. Zharnikov and M. Grunze, *J. Vac. Sci. Technol. B*, 2002, **20**, 1793-1807.
60. A. Turchanin and A. Gölzhäuser, *Prog. Surf. Sci.*, 2012, **87**, 108-162.
61. I. Horcas, R. Fernandez, J. M. Gomez-Rodriguez, J. Colchero, J. Gomez-Herrero and A. M. Baro, *Rev. Sci. Instrum.*, 2007, **78**.
62. J. F. Moulder, W. E. Stickle, P. E. Sobol and K. D. Bomben, *Handbook of X-ray Photoelectron Spectroscopy,*, Perkin-Elmer Corp.: Eden Prairie, MN, 1992.

63. J. Stöhr, *NEXAFS Spectroscopy*, Springer, 1992.
64. P. E. Batson, *Phys. Rev. B*, 1993, **48**, 2608-2610.

